Journal of Materials Chemistry A

ROYAL SOCIETY OF CHEMISTRY

PAPER

View Article Online
View Journal

Cite this: DOI: 10.1039/d5ta06611e

Complex influence of stack pressure on BiF_3 cathode materials in all-solid-state fluoride-ion batteries

Hong Chen, Pervin Bal and Oliver Clemens *

Among all the alternative battery systems beyond lithium-ion batteries (LIBs), all-solid-state fluoride ion batteries (ASSFIBs) are particularly promising due to their high theoretical energy density, thermal stability, and recent advancements in room-temperature superionic solid electrolytes and intercalation-type electrodes. However, their practical application is hindered by poor cycling stability and limited rate capability, largely attributed to unfavored kinetics and interfacial degradation, especially in conversion-type cathodes. Previous studies have shown that the application of stack pressure can significantly improve the cell's cycling stability. To reveal the underlying mechanism, this study systematically investigates the impact of stack pressure on the electrochemical performance of ASSFIBs using $BiF_3|BaSnF_4|Sn$ cells. Among the tested conditions, the best enhancement of cycling stability and rate performance was demonstrated under 180 MPa. Furthermore, *ex situ* diffraction analysis revealed pressure-dependent phase evolution and oxygen-related interfacial degradation (*i.e.*, BiOF or $BiO_{0.1}F_{2.8}$ formation) in the BiF_3 cathode during the first cycle. Through *in situ* electrochemical impedance spectroscopy combined with distribution of relaxation times analysis we identified charge transfer and F^- diffusion as the dominant state-of-charge dependent kinetic limitations, with strong correlation to phase transitions within the BiF_3 cathode composite. These findings emphasize the critical role of stack pressure in mitigating interfacial degradation and optimizing ion transport, providing valuable insights for the design and operation of high-performance ASSFIBs.

Received 14th August 2025
Accepted 15th November 2025

DOI: 10.1039/d5ta06611e

rsc.li/materials-a

1 Introduction

The widespread adoption of Li-ion batteries (LIBs) in transportation devices and renewable energy storage systems has reshaped society over the last few decades and promises a sustainable future. However, the flammability of liquid electrolytes and the high cost of critical raw materials for LIBs have motivated a technological shift towards all-solid-state batteries (ASSBs) and systems employing alternative shuttle ions, such as Na^+, Mg^{2+}, Cl^- and F^-, to meet the ever-increasing demands of large-scale energy storage. Recently, all-solid-state fluoride-ion batteries (ASSFIBs) are becoming more competitive due to their high theoretical energy density up to ~5000 Wh L^{-1} using metal fluorides as electrodes,[1,2] thermal stability, and progress in developing superionic solid electrolytes at room temperature and intercalation-based electrode materials such as La_2CoO_4, La_2NiO_4, $La_{2-x}Sr_xMnO_4$ and their derivatives.[3–7]

However, in practical application, the potential of ASSFIBs is hindered by poor cycling stability, limited rate capability, unfavored diffusion and/or reaction kinetics, and interfacial degradation. These limitations can be broadly attributed to two key processes: mechanical inter-particle contact loss (suddenly or progressively) and chemical decomposition at the interfaces.[8,9] Unlike liquid electrolyte systems, where mechanical accommodation occurs more easily, all-solid-state batteries (ASSBs) are subjected to mechanical constraints, from fabrication to operation. Even minor volume fluctuations in active materials can bring substantial internal stress into the system.[10] In ASSFIBs, particularly for conversion-based cathode materials, the reduction of metal fluorides (which can be described by $MF_y + ye^- \rightarrow M + yF^-$) accompanied by large volumetric changes ($\Delta V \approx 30$–70%) will lead to severe delamination within the composite. This can result in poor electronic/ionic percolation, increased overpotential, and ultimately, rapid capacity fading. Furthermore, interface instability between the electrode and solid electrolyte appears to dominate the cell performance in ASSBs, even more than in conventional lithium-ion batteries (LIBs), since the undesirable reaction products cannot dissolve and diffuse in the solid electrolyte.[11]

To overcome these challenges, many strategies have been explored, including the optimization of the electrode composite and interfacial engineering.[12–17] Among them, applying stack pressure has shown significant benefits by mitigating the inter-particle contact loss and partially stabilizing interfacial

University of Stuttgart, Institute for Materials Science, Materials Synthesis Group, Heisenbergstraße 3, 70569, Germany. E-mail: oliver.clemens@imw.uni-stuttgart.de; Fax: +49 711 685 51933

reactions.[18–23] The effects of stack pressure appear to be system-specific, depending on the chemical & mechanical properties of the electrode-solid electrolyte interface. In all-solid-state lithium-ion batteries (ASSLIBs), numerous studies have shown the pressure-dependent improvement originates from various mechanisms. For example, the ionic conductivity of Li_3InCl_6 increases from 0.35 to 0.52 mS cm^{-1} when pressure is raised from 2 to 10 MPa at 30 °C, which in turn enhances the utilization of cathode active materials such as single-crystal $LiNi_{0.83}Mn0_{.06}Co_{0.11}O_2$, leading to 93% capacity retention after 50 cycles at 10 MPa, compared to 65% at 2 MPa.[21] Many works have also reported that the intrinsic volume change of electrode active materials determines the critical stack pressure to maintain an intimate and effective interface to achieve sustained cycling. For instance, silicon anodes (up to 300% volume expansion upon lithiation) require a stack pressure of 50–120 MPa,[24,25] while Nb_2O_5 with 4% expansion only needs a minimum stack pressure of 2 MPa to reach capacity retention above 96% over 30 cycles.[22] In contrast, zero-strain cathodes like $Li_4Ti_5O_{12}$ (LTO) can maintain coulombic efficiency above 99% under a minimal pressure of 0.1 MPa.[22]

Our previous study extensively investigated the pressure-dependent conductivity of various solid electrolytes for ASSFIBs and demonstrated significant improvements in electrochemical performance for conversion-based and intercalation-based electrodes under applied stack pressures.[18] However, the mechanism underlying the effects of stacking pressure on ASSFIBs remains unexplored. In solid-state batteries, electrode–electrolyte interfacial degradation has been studied using techniques such as XPS, TOF-SIMS, and TEM. Alongside these methods, electrochemical impedance spectroscopy (EIS) has significant advantages as a non-destructive tool for probing interfacial kinetics under *operando* conditions. While equivalent circuit modelling (ECM) of impedance spectra has traditionally been used for data interpretation, its application in ASSBs is limited by overlapping impedance features with similar time constants and difficulty in distinguishing electrode contributions. In recent years, distribution of relaxation times (DRT) analysis has been extensively applied in LIBs research,[26–30] and its application is becoming increasingly important in ASSBs. By converting impedance data into the time domain without circuit assumptions, DRT can reveal distinct relaxation processes, such as charge transfer, ion diffusion, and interphase formation, with high resolution, enabling clearer interpretation of complex interfacial phenomena.

In this work, we report on the pressure-dependent cell performance of a BiF_3 cathode composite. The first-cycle performance under varying pressure is investigated, in addition to determining cycling stability and C-rate capability under the optimized stack pressure condition. Furthermore, *operando* X-ray diffraction (XRD) and *ex situ* XRD analysis are used to investigate the phase evolution of the BiF_3 cathode in BiF_3-$|BaSnF_4|Sn$ cells. In addition, *in situ* EIS with DRT analysis is employed to study the state-of-charge (SOC) and pressure dependence of different polarization processes, including charge transfer and ion diffusion. The results reveal the complex multi-scale effects of stack pressure, from crystalline phase formation and O^{2-}/F^- diffusion to macroscopic interfacial behavior, which then collectively influence the overall cell performance.

2 Experimental

2.1 Material synthesis

Barium fluoride (BaF_2) (99.99%) and tin fluoride (SnF_2) (99%) from Sigma Aldrich were used for synthesizing electrolyte $BaSnF_4$ by mechanical milling and post soft annealing. All starting materials were dried in a vacuum furnace inside an argon-filled glovebox to remove any absorbed moisture. Stoichiometric amounts (~3 g in total) were sealed in a ZrO_2 milling vial (50 mL) with ZrO_2 milling balls (5 mm diameter, ball-to-powder ratio of 17 : 1) under an argon atmosphere in the glovebox and milled at 600 rpm for 4 h using a Retsch Planetary Ball Mill PM100. After ball milling, the powder mixture was annealed at 300 °C for 2 h under dynamic vacuum (10^{-2} mbar) using a Büchi Glass Oven B-585. The mechanical milling and the annealing process were repeated three times to enhance the doping process. Bismuth trifluoride (BiF_3) (99%) from Alfa Aesar, Sn nanopowder (>99%, <150 nm particle size (SEM)) and carbon nanofibers (CNF) (>98%) from Sigma Aldrich were used to prepare the BiF_3 cathode and Sn anode composites, as described by Reddy *et al.*[31] The cathode composite consisted of 40 wt% BiF_3, 50 wt% $BaSnF_4$, and 10 wt% CNF, while the anode composite contained 50 wt% Sn, 40 wt% $BaSnF_4$, and 10 wt% CNF. Again, BiF_3 and CNF were dried at 190 °C under dynamic vacuum for 24 h using the vacuum furnace before the synthesis process.

2.2 Cell assembly and electrochemical measurements

Cell pellets were prepared in a three-layer configuration by uniaxially pressing the anode composite, electrolyte, and cathode composite using a Specac Atlas 25T manual hydraulic press in an argon-filled glovebox (2 *t* for 90 s). The mass loadings of electrolyte, anode composite and cathode composite were 200 mg, 10 mg and 5 mg, respectively, *i.e.*, the anode composite was used in excess relative to the cathode composite. The galvanostatic cycling was performed at 100 °C in the potential range from 0.05 to 1 V (*vs.* Sn/SnF_2) with a current density of 20 μA cm^{-2} (unless specified otherwise) on potentiostats from Biologic Science Instruments (VSP or VMP-300 for cycling and VSP-300 for *operando* XRD measurements). The specific capacities were calculated based on the weight of the active material in the cathode composite (BiF_3). For the C-rate capability test, a staircase increase of the C-rate (0.02C, 0.5C, 0.1C, 1C) was selected and conducted for three cycles each, after 15 consecutive cycles at 0.01C.

For galvanostatic cycling under different stack pressures, cells were assembled and tested directly in the customized hot-press setup.[18] The disc springs were used to minimize the force changes due to dynamic volume change of the pellet during cycling. Stack pressure variation between 20 and 450 MPa was studied due to the stable pressure range of the disc springs

used. The chosen electrolyte was first filled in and compacted by hand. Afterwards the anode composite was hand-compacted on one side of the electrolyte and the cathode composite on the other side. The cells were compacted at 450 MPa for 90 s in a housing module made of Al_2O_3 (inner diameter 7.5 mm, corresponding to a cell area of 0.441 cm^2) which then sits inside a steel mantle for radial constraint of the alumina housing. A pair of cylindrical hot working steel pins (AISI H11, 7.5 mm in diameter) were used as the current collector, which were aligned and electronically insulated by additional PTFE tubes. The entire hot-press setup was placed inside an argon-filled glovebox for operation under an inert atmosphere to avoid possible material degradation which can be induced by the presence of humidity and/or oxygen. Before cycling, the cell was heated up to the desired temperature and held for at least 4 h to reach thermal equilibrium. A pre-stack pressure which is slightly lower than the desired value was applied on the cell before heating, to minimize internal delamination due to thermal expansion, and the actual stack pressure after thermal equilibration was calculated from the recorded on-site force and adjusted accordingly. Cells cycled in typical high-temperature Swagelok type cells[31] (~0.2 MPa) are referred to as non-pressure cells within this manuscript. To investigate the phase evolution of BiF_3 during charging, *operando* XRD measurements during galvanostatic cycling were conducted at 100 °C, and a Swagelok-type cell of compact design was used,[32] where the pressure applied to the cell was estimated to be less than 0.1 MPa. The detailed description of *operando* XRD measurements can be found in chapter 2.3.

To evaluate the SOC and pressure-dependent interfacial degradation of the BiF_3 cathode composite, EIS was performed under various stack pressures using VSP or VMP-300, after 2 h of galvanostatic cycling at 40 μA cm^{-2} and the following 2 h of rest (open-circuit voltage (OCV) monitoring). Impedance spectra were recorded at the open circuit state using a signal amplitude of 10 mV in the frequency range of 1 MHz to 100 mHz. DRT analysis was performed using RelaxIS 3 from rhd instruments. The DRT transformation with Gaussian radial basis function (RBF)-based discretization was conducted to deconvolute the complex impedance data. The second derivative of the distribution function was used as the penalty item for all patterns in this work, with a shape factor value of 0.5 and regularization parameter $\lambda = 10^{-7}$. The obtained DRT patterns with multiple peaks were fitted using Gaussian functions to determine the characteristic time constants and peak areas. More details are provided in the literature.[28]

2.3 X-ray diffraction

A Rigaku SmartLab diffractometer with a Cu K$\alpha_{1,2}$ radiation (40 kV, 30–40 mA) source and a HyPix-3000 detector was used to characterize the crystal structure of the synthesized electrolyte, cathode and anode composites as well as cell pellets after galvanostatic cycling in Bragg–Brentano geometry.

For *ex situ* X-ray diffraction experiments, powder samples or cell pellets released from ceramic modules at different SOCs were placed in low background airtight sample holders inside an argon-filled glovebox. X-ray diffraction (XRD) patterns were recorded at room temperature, with an incident slit size of 0.3°. A step size of 0.005° was applied in the 2θ range from 10° to 80°, leading to a total measurement time of 2 h 35 min. Since the phase evolution of the cell investigated during discharge has been demonstrated in our previous study,[32] *operando* XRD patterns were recorded at 100 °C on a cell pellet (cathode side) in the discharged state (pre-discharged to 0.05 V against Sn/SnF_2) while galvanostatic charging was performed in this work. The 2θ range was limited to 21.5–40.5° with a step size of 0.005° (and a scan time of 26 min). To obtain sufficient time-resolved data allowing for both phase analysis and quantification, a loop measurement was programmed to record XRD patterns during the galvanostatic charge process, at 1 h intervals. More details about the *operando* measurement can be found in our previous publication.[32]

Rietveld analysis of the diffraction data was performed using TOPAS V6,[33] using a fundamental parameters approach as described in the literature,[6] with the instrumental broadening being derived from a reference scan on a NIST standard of LaB_6 (660a). To refine the different crystal structures of BiF_3, Bi, and oxidefluorides, crystallographic information, as reported in the literature,[34–37] was used without adjusting the atomic positions, but allowing for the refinement of lattice parameters. The structural model for the orthorhombic modification o′-$BiF_{3-\delta}$ was derived as described in the literature.[32] To account for angular dependent broadening effects from crystallite size and micro strain in the individual phases, two Voigt functions were used. An identical thermal displacement parameter of all atoms of all phases was constrained to minimize quantification errors. Batch Rietveld analyses were performed on *operando* XRD patterns by a python script which repeats the fitting process with the pre-refined boundary values and constraints carefully set on parameters in Topas V6 software to the group of patterns.

3 Results and discussion

3.1 Pressure effects on cell performance

3.1.1 Cell performance during the first cycle under various stack pressures. Fig. 1 shows the relation between the first-cycle behavior of the BiF_3 composite and stack pressures. The dQ/dV plots of the cells under various stack pressures during (dis) charge are summarized in Fig. 1a, with detailed features within the selected voltage range demonstrated in Fig. 1b–e. It can be seen that the peaks in the dQ/dV curves show strong changes with stack pressure. With an increase in stack pressure from 24 MPa to 221 MPa, the cell overpotential, represented by the difference between redox reaction plateaus during (dis) charging, reduces by approximately 50 mV (marked by the blue arrow in Fig. 1b, d and e). This is indicated by the peaks corresponding to reduction reaction plateaus in the dQ/dV plots, which shift toward higher values (Fig. 1d and e), and the peaks corresponding to oxidation reaction plateaus, which shift to lower values (Fig. 1b). However, upon further increasing the pressure to 410 MPa, the overpotential begins to rise again (marked by the red arrow in Fig. 1b, d and e). The corresponding specific capacities of all cells are plotted in Fig. 1f, and the

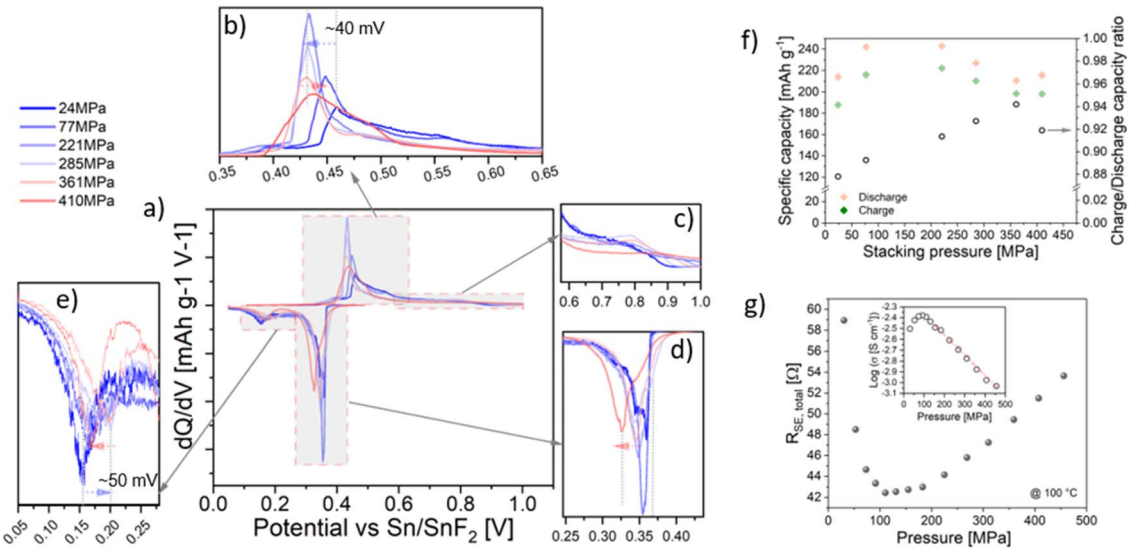

Fig. 1 (a) dQ/dV plot of the BiF_3|$BaSnF_4$|Sn cells during the first (dis)charge cycle (at 100 °C, current density of 40 μA cm^{-2}) under different stacking pressures and selected zoomed-in features (b–e), corresponding potential profiles against capacity are given in Fig. S1; (f) pressure dependent specific capacity of the (dis)charge process and charge/discharge capacity ratio of the cells in (a); (g) pressure dependent total resistance of solid electrolyte $BaSnF_4$ at 100 °C; the inset is the logarithm of the corresponding ionic conductivity against pressure.

charge-to-discharge capacity ratio was calculated to evaluate the cell efficiency. Both discharge and charge capacity are enhanced with stack pressure up to 221 MPa, and decrease with further increasing the pressure, leading to a consistent increase in coulombic efficiency. This observed behavior in the cell overpotential and the (dis)charge capacity correlates well with the pressure-dependent ionic conductivity of the solid electrolyte $BaSnF_4$. Fig. 1g shows the total resistance (bulk and grain boundary contribution are not distinguishable; representative EIS measurement is provided in Fig. S2) of the pure electrolyte (200 mg) under different pressure conditions obtained by electrochemical impedance measurement, between 14 and 450 MPa, which reflects directly the contribution of the electrolyte layer to the polarization process. The logarithm of the ionic conductivity of $BaSnF_4$ is plotted as a function of pressure as the inset, where the linear decrease in ionic conductivity of $BaSnF_4$ with pressure is explained by the so-called activation volume of the electrolyte, *i.e.*, the intrinsic ionic conduction properties of the electrolyte.[18,38] The increase in the electrolyte resistance in the low-pressure range is attributed to loss of contact at the pellet interface with current collectors and within the pellet itself (crack formation due to the elastic recovery of the pellet). Furthermore, the DC polarization measurement of $BaSnF_4$ at 100 °C under varied pressure conditions lacks pressure dependency of its electronic conductivity (which is low in the order of 10^{-9} S cm^{-1}), which rules out an electronic contribution to the observed conductivity trend (Fig. S3). More details on the pressure effects on $BaSnF_4$ and other solid electrolytes in ASSFIBs are provided in our previous study.[18] In SSBs, ion conduction of the solid electrolyte and, if applicable, through solid electrolyte interfaces (SEIs), is typically static and SOC-independent. Therefore, their contribution can be more easily identified.[39] A similar relationship was reported by Gao *et al.*[21] in ASSLIBs, where a strong correlation between ionic conduction of the electrolyte and the achievable cell capacity was demonstrated. Consistent with these findings, our results indicate that in ASSFIBs based on a BiF_3 cathode, the effect of stack pressure on cell capacity primarily arises from its influence on the pressure-dependent ionic conduction performance of the electrolyte, which is reflected by shifts in redox reaction plateaus.

3.1.2 Cell performance under high stack pressure. To evaluate the long-term impact of stack pressure on the BiF_3-|$BaSnF_4$|Sn cell, galvanostatic cycling was conducted at 100 °C under a constant stack pressure of 180 MPa (selected based on the first-cycle cell performance in chapter 3.1.1) using a current density of 20 μA cm^{-2}. Our previous study demonstrated that for a sufficiently high charge cutoff potential, stack pressure can induce a second plateau around 1.1 V, which could be attributed to side reactions related to fluorination of the stainless steel pin or CNF.[18] Therefore, in this work, a charge cutoff condition of 1 V was chosen to avoid undesired side reactions. Fig. 2a and c demonstrates the potential profile against capacity of the pressure cell and compares the corresponding coulombic efficiency (CE) and energy efficiency (EE) of both cells. The CE is determined by the ratio of the charge capacity to the discharge capacity from the previous cycle. It can be clearly seen that, in agreement with the findings of our previous study,[18] the cell under 180 MPa (Fig. 2a) exhibits remarkable stability, retaining a discharge capacity of ~115 mAh g^{-1} (approximately 50% of the initial discharge capacity) after 15 cycles, with negligible change in overpotential (*i.e.*, stable flat voltage plateaus). In contrast, the cell under non-pressure conditions (see Fig. S4) shows a rapid increase in overpotential with cycling, resulting in a drastic capacity fade to below 50 mAh g^{-1} (17% of the initial value) within just 10 cycles. In Fig. 2c, the cell under high stack

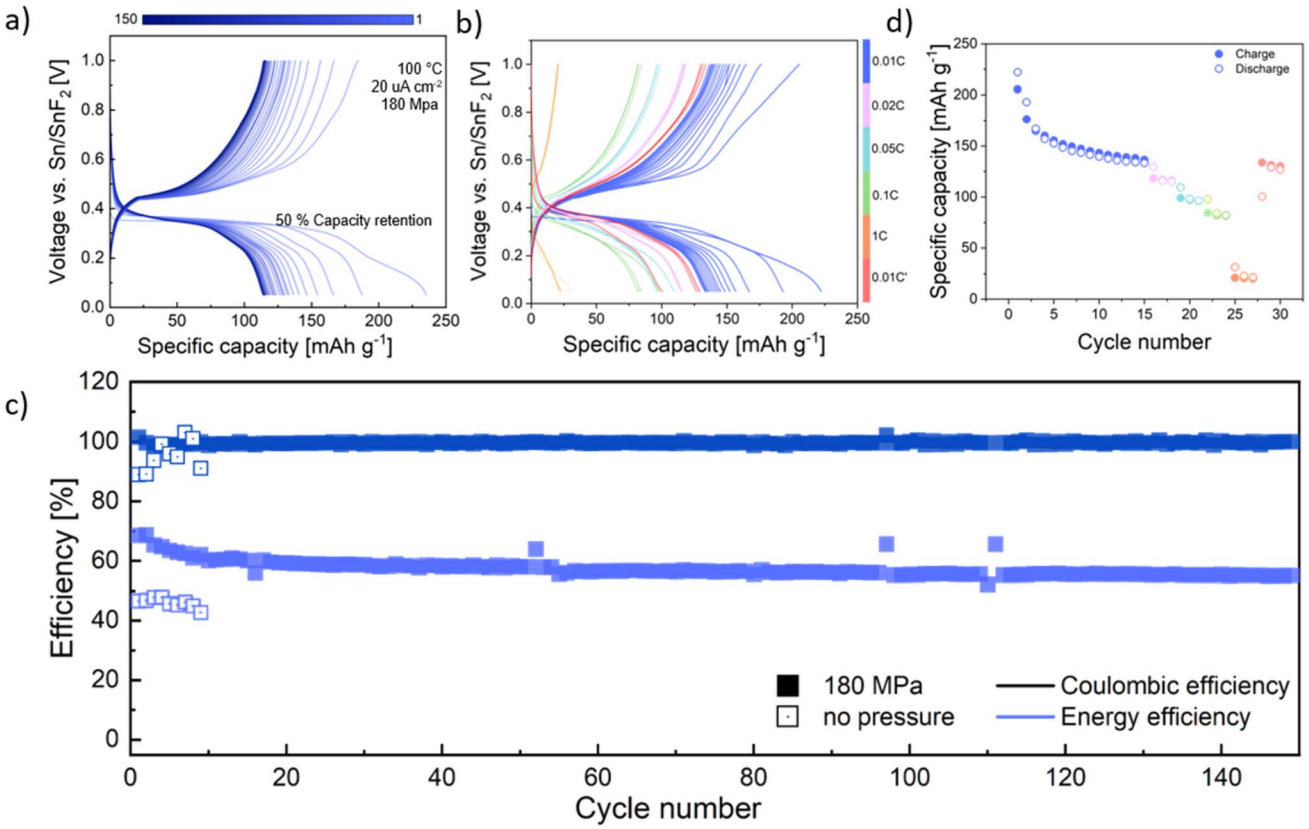

Fig. 2 The (dis)charge profiles of the cells cycled at 20 μA cm^{-2} under 180 MPa stack pressure in a hot-press setup (a) and (c) corresponding coulombic and energy efficiency; (b) selected C-rate test of the cell under a stack pressure of 180 MPa at 100 °C and the corresponding capacity retention (d). 0.01C′ refers to the measurements at 0.01C after cycling at 1C (302 mA g^{-1}).

pressure maintains a CE above 98% over 150 cycles and exhibits an EE improvement of a factor of approximately 1.5 compared to the non-pressure cell. This pronounced performance enhancement can be attributed to the mitigation of interfacial degradation mechanisms in the pressurized system. In ASS-FIBs, large volume change during the conversion reaction, in this case $BiF_3 + 3e^- \rightarrow Bi + 3F^-$ ($\Delta V = 29$–40%, depending on the modification of BiF_3),[37,40,41] can induce mechanical delamination at the solid–solid interfaces, leading to sudden or progressive loss of contact, increased impedance and inaccessibility of the cathode active material. Our previous study[18] reported that high stack pressure significantly helps to improve the cell's mechanical integrity, which mitigates contact loss between solid–solid particles and preserves the electronic and ionic percolation pathway, thereby ensuring sustained access to electrochemically active BiF_3 particles throughout cycling. The comparison of the cross-section SEM images of $BiF_3|BaSnF_4|Sn$ cells after cycling with no pressure and 180 MPa is provided in Fig. S5. Furthermore, Fig. 2b and d demonstrate the C-rate capability of the cell under a stack pressure of 180 MPa. While the internal resistance (IR) drop increases with current density as expected, additional kinetic limitations appear to influence capacity retention. Notably, the observed capacity decay with increasing current density is mostly reversible upon returning to low currents. This effect is particularly more pronounced during charging and becomes more evident in the later stages of charge at high C-rates, indicating the presence of SOC-dependent processes, such as dynamic phase evolution and solid interphases from interfacial degradation at the electrode–electrolyte interface.

3.2 Oxidefluoride formation under different stack pressures

As previously reported,[32] BiF_3 cathodes undergo a complex phase evolution during discharge at 100 °C, transitioning sequentially from orthorhombic BiF_3 (o-BiF_3) to cubic BiF_3 (c-BiF_{3-x}) and then to a defect-rich orthorhombic phase (o′-$BiF_{3-\delta}$), before forming metallic Bi. To further investigate the reversibility of this process, *operando* X-ray diffraction (XRD) was performed on the $BiF_3|BaSnF_4|Sn$ cell upon charging, using identical temperature and current conditions. As shown in Fig. S6, *operando* XRD reveals partial reversibility of BiF_3 and the detrimental role of oxidefluoride formation during discharge. Starting from the discharged state (cell potential of 0.05 V), the metallic Bi ($R\bar{3}m$) was fluorinated following the reverse pathway to discharging, initially forming o′-$BiF_{3-\delta}$ ($Fmmm$), followed by c-BiF_{3-x} ($Fm\bar{3}m$), with increasing F^- insertion into the lattice. This process is evidenced by the coherent increase in weight fraction of both phases observed. However, the oxidefluoride BiOF ($P4/nmm$) formed during discharging was found to be electrochemically inactive once formed and persists throughout

the charging process. This is attributed to the thermodynamically stable nature of the Bi–O bond under cell operating conditions (100 °C), which makes F^-/O^{2-} exchange highly unfavorable. Also, oxygen diffusion is sluggish at solid–solid interfaces compared to fluoride ion diffusion, further limiting the reversibility.[32] Furthermore, when the cell is charged to 1 V, no orthorhombic BiF_3 (*Pnma*) was observed, and the cell volume of the formed c-BiF_{3-x} (~195.9(2) Å^3) is smaller as compared to the initial value (~199.2(2) Å^3) observed before the first discharge process.[32] This likely indicates a defect-richer structure and plausible oxygen incorporation in the cubic phase during charging.[42]

To understand the effects of stack pressure on the phase evolution, *ex situ* XRD was conducted on cells charged to 1 V after cycling under various stack pressures. Fig. 3a compares the *ex situ* XRD patterns of those cells, and it can be seen, from the reflections marked by grey rectangles in Fig. 3a, that the phase evolution of $BiF_{0.1}O_{2.8}$ in the BiF_3 cathode exhibits pressure-dependent behavior. As obtained from detailed Rietveld analysis, the relative weight fraction of Bi-containing phases in the BiF_3 cathode composite is shown in Fig. 3b (Partial fits are given in Fig. S7 and S10). In contrast to non-pressure conditions, even when only a moderate pressure of 20 MPa is applied, BiOF can no longer be detected; instead a F^--rich oxidefluoride $BiO_{0.1}F_{2.8}$ phase[35] (*P*6$_3$/*nmm*, $a = 4.083$ Å, $c = 7.323$ Å) is observed. This phase is structurally and chemically distinct to orthorhombic[37] and cubic BiF_3 modifications[32] and BiOF[35] (*P*4/*nmm*, $a = 3.746(9)$ Å, $c = 6.226(1)$ Å), but has a very similar powder XRD pattern to trigonal BiF_3 (ref. 43) ($P\bar{3}c$, $a = 7.165$ Å, $c = 7.318$ Å). However, there is a very strong difference in the unit cell volumes that have been observed for those phases. As an example, the overview of crystallographic data of BiF_3 and oxyfluorides obtained in the partial fit of the BiF_3 cathode composite of a cell pellet (dis)charged (0.05–1 V) under a pressure of 180 MPa (Fig. S8) is listed in Table S1. The volume per BiO_xF_{3-2x} ($0 \leq x \leq 1$) unit in trigonal BiF_3 and the compound observed by us is very different by ~2.6%, whereas the

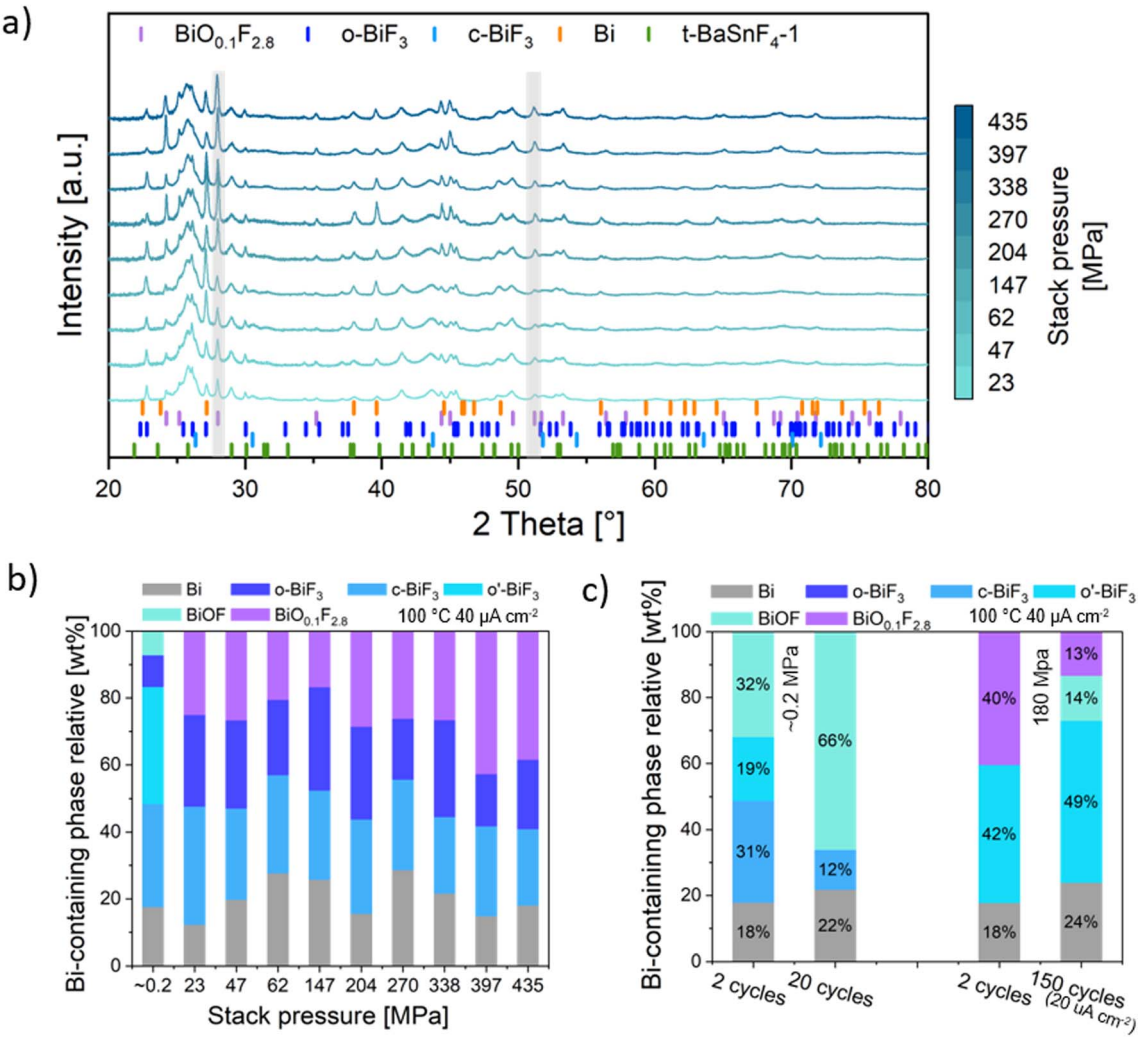

Fig. 3 (a) Comparison of XRD patterns of the cells cycled at 100 °C with 40 µA cm^{-2} under different stack pressures for 1 cycle (charged to 1 V). Reflections marked by grey rectangles correspond to $BiF_{0.1}O_{2.8}$ (1 0 1) and (2–1 2); (b) phase analysis of the cells in (a), with comparison of non-pressure cell; (c) phase analysis of the cells cycled at 100 °C with 40 µA cm^{-2} (20 µA cm^{-2} for the 150 times cycled cell) for 2 cycles and long-term cycle. Corresponding partial fits are given in Fig. S7 and S10.

orthorhombic modification observed fits with the volume within error (~−0.07% volume difference to what has been reported in the literature[37]), and the smaller difference of the cubic modification is explained by its defect richer nature (as outlined in detail in our previous article[32]). A volume difference of 2.6% for a symmetry distorted variant must thus have another origin. Given the volume evolution of BiO_xF_{3-2x} on oxygen substitution (Table S2 and Fig. S9) appears a fairly linear dependence on the oxygen content x in the BiO_xF_{3-2x} unit, the lattice parameters and volume we observed are very much in agreement with the reported hexagonal modification of $BiO_{0.1}F_{2.8}$, giving even a better fit with a reduced R_{wp} value (in Table S1). Both our previous study[32] as well as this work have shown that in the pressure-free cells the presence of the tetragonal modification of BiOF (with a very low volume per BiO_xF_{3-2x}) is unquestionable. Since O substitution is thus a known phenomenon to occur within the cathode composite,[32] the identification of the low-O content bismuth oxyfluoride $BiO_{0.1}F_{2.8}$ with clearly different volume per BiO_xF_{3-2x} unit than trigonal BiF_3 is conclusive. However, one should be aware that the oxygen content cannot be determined precisely here, but that an overall fluorine-rich composition is indicated. Interestingly, the formation of $BiO_{0.1}F_{2.8}$ is contradictory to the mechanism for the formation of BiOF at the later discharge stage, which involves introduction of F^- defects into BiF_3 and accumulation of oxygen impurity during defluorination.[32] To clarify the origin of $BiO_{0.1}F_{2.8}$, cells cycled under 20 MPa and 180 MPa were analyzed by *ex situ* XRD at the discharged state (cell potential of 0.05 V). As shown in Fig. S11, no BiOF or $BiO_{0.1}F_{2.8}$ is detected at the discharged state, suggesting that $BiO_{0.1}F_{2.8}$ most likely forms under pressure in the later stage of charging (considering its fluorine-rich composition). This finding implies that stack pressure affects oxygen transport kinetics in the BiF_3 composite; especially, O^{2-} diffusion appears to be suppressed within the investigated pressure range, which is critical for phase evolution.

Notably, the pressure-dependent formation of $BiO_{0.1}F_{2.8}$ appears to be closely correlated with the ionic conductivity trend of $BaSnF_4$ discussed in Section 3.1. With increasing stack pressure from 20 MPa to 150 MPa (in Fig. 3b), a reduced weight fraction of $BiO_{0.1}F_{2.8}$ is observed, and with a further increase in applied pressure, the amount of $BiO_{0.1}F_{2.8}$ rises again. This observation indicates the formation of $BiO_{0.1}F_{2.8}$ to be a consequence of the interplay between the kinetics of F^- and O^{2-} diffusion and their different activation volumes within the BiF_3 cathode composite, which result in different pressure dependencies of the fluoride and oxide ion transport. Pure fluorides are in general poor oxygen conductors and, to the best of our knowledge, there is no study on oxygen conduction (and pressure dependency) within $BaSnF_4$ or other fluorides so far. However, many studies on the activation volume for O^{2-} in fluorite-type oxides and F^- in fluorite-type (-related) fluorides have been reported.[18,44] Christopoulos *et al.*[44] reported that the activation volume of O^{2-} diffusion in fluorite structured oxides (ThO_2, UO_2 and PuO_2) at room temperature locate in the range of 10^{-14} cm^3 mol^{-1}. Even for a superior oxide conductor ZrO_2 (doped with 8 mol% Y_2O_3),[45] the activation volume for O^{2-} transport at 750 °C is 2.08 cm^3 mol^{-1}. In our previous study,[18] the determined activation volume of F^- in $BaSnF_4$ is 1.01(2) cm^3 mol^{-1} at 30 °C. Given that the activation volume of O^{2-} diffusion is significantly higher than that of F- diffusion due to its larger ionic radius and higher covalency, our observation of reduced formation of bismuth oxyfluorides under pressure conditions is well in line with this behavior, suggesting that the O^{2-} diffusion process is considerably more sensitive towards stack pressure than F^- diffusion within the cathode composite. In addition, by studying low-pressure cells using *operando* XRD it is confirmed that the O species in the composite contribute to the formation of BiOF during discharging by a plausible F^-/O^{2-} exchange mechanism at electrode–electrolyte interfaces.[32] Therefore, under stack pressure the eliminated voids and the improved contact between particles would certainly affect the O^{2-} diffusion at the interfaces. In summary, we interpret the pressure-dependent formation of $BiO_{0.1}F_{2.8}$ as follows: from 20 MPa to 450 MPa, the solid–solid contact has been improved by increasing pressure and thus reducing the availability of the interfacial pathway for O^{2-} diffusion in the cathode composite, while F^- transport is still dominated by the solid electrolyte. Initially, as the pressure increases from 20 MPa to 150 MPa, the suppression of O^{2-} diffusion combined with enhanced F^- transport leads to reduced formation of $BiO_{0.1}F_{2.8}$. At pressures beyond 200 MPa, the ionic conductivity of $BaSnF_4$ significantly drops, limiting F^- transport to a level more comparable with O^{2-} diffusion. As a result, the weight fraction of the $BiO_{0.1}F_{2.8}$ phase increases again slightly, possibly indicating a pressure threshold beyond which F^- transport becomes a rate-limiting factor for oxyfluoride formation.

It is important to note that oxygen accumulation is a continuous process during cell operation, particularly in the system where the solid electrolyte is the main source of oxygen impurity.[32] Given that, prolonged cycling would unavoidably lead to an increase of oxidefluoride content. This agrees with the findings reported in Fig. 3c, which compares the weight fraction of Bi-containing phases of cells under non-pressure conditions and constant pressure of 180 MPa after cycling. After 20 cycles without stack pressure, BiOF accounts for approximately two thirds of the Bi-containing phases. This finding is consistent with the severely decayed capacity to below 10% of the theoretical value of 302 mAh g^{-1}. In contrast, under 180 MPa, oxygen accumulation is significantly suppressed, and with prolonged cycling its negative impact becomes pronounced. After 150 cycles, partial transformation of $BiO_{0.1}F_{2.8}$ to BiOF is observed, indicating gradual interfacial degradation. This observation is well reflected in the cell capacity decay observed in Fig. 2a, confirming that by applying optimized pressure, the oxygen-accumulation-related degradation can be significantly reduced, but not eliminated. Thus, these results reveal a dual impact of stack pressure, promoting F- diffusion and suppressing O^{2-} transport. Nevertheless, the presence of oxygen impurities remains a critical limitation, especially in long-term cycling, even at optimized pressure ranges. This emphasizes the importance of solid electrolyte purity, improved interfacial design and cell fabrication for ASSFIBs.

3.3 *In situ* EIS-DRT analysis under different stacking pressures

As discussed in Section 3.1, the effect of stack pressure on the BiF_3 cathode in ASSFIBs is closely related to the pressure-

dependent ionic conductivity of $BaSnF_4$, as reflected by the shift of the flat voltage plateaus. However, cycling performance under pressure also reveals additional, non-negligible contributions from kinetic limitations, particularly evident at later SOCs and correlating with the observed capacity decay. Such kinetic limitations are primarily attributed to charge transfer and ion diffusion processes within Bi-containing active materials, both of which are typically dynamic processes and SOC-dependent, each with distinct time constants which can be probed by EIS. To further understand these processes, *in situ* EIS-DRT analysis was conducted at different OCVs during the first cycle under three pressure conditions as used for the cell characterization: moderate (20 MPa, Fig. 4a), high (180 MPa, Fig. 4b), and ultra-high (430 MPa, Fig. 4c). The evolution of the Impedance spectra during discharge and charge during OCV monitoring is shown in Fig. 4a–c next to the corresponding cell potential profiles, respectively. The corresponding DRT patterns are given in Fig. 4d–f, indicated with specific time constant regimes. In particular, the SOC-dependent interfacial processes, which could be identified and categorized based on a comparison to literature values of typical kinetics processes in solid-state batteries[26,28] (one example of peak fitting and more comments on categorization are shown in Fig. S12), are plotted against the OCV in Fig. 5a and b, and the detailed values are listed in Tables S3 and S14.

As can be seen in Fig. 5a and b and the corresponding DRT plots shown Fig. 4d–f, the single peak with the highest intensity in the τ_3 (>1 s) regime is attributed to the F^- ion diffusion in the polycrystalline Bi-containing electrode materials (including bulk and grain boundary contributions). The less pronounced peaks located in the faster τ_2 (10^{-2}–10^0 s) regime correspond to the charge-transfer processes of both electrodes. These peaks also reflect the microstructural changes at electrode–electrolyte interfaces with a change of SOCs. In the τ_1 (10^{-5}–10^{-2} s) regime, we assign the smaller peak to the charge transfer across any interphases. In the τ_0 (<10^{-5} s) regime, contributions from solid electrolyte (*i.e.* contributions from both bulk and grain boundary responses of the nanocrystalline $BaSnF_4$ electrolyte, hereafter referred to as R_{SE}) and the potential contact resistance with the current collector are present. Due to the absence of a semicircle corresponding to $BaSnF_4$ within the measured frequency range, the R_{SE} was determined by the intercept of Nyquist plots on the real impedance axis and excluded from DRT fitting (Fig. S12). For all three pressure conditions, R_{SE} reveals a nearly constant value during both defluorination and fluorination, indicating SOC independence as would be expected for an electrolyte; the detailed values are listed in Tables S3 to S14.

To confirm the dominance of BiF_3 cathode-related kinetic processes, a control EIS-DRT measurement was performed on a Sn/SnF_2 symmetric cell in the half fluorination state (Sn to SnF_2 mass ratio is 1 : 1) and after 20 cycles (Fig. S13). It is found that such a Sn anode retains a relatively stable overpotential (slowly growing to 15 mV over 24 cycles); its contribution to the $BiF_3|BaSnF_4|Sn$ cell can thus be considered to be negligible. Furthermore, though the Sn/SnF_2 electrode exhibits similar time constants to the BiF_3 cathode, compared to BiF_3, the evolution of the peak's intensity is small and the corresponding resistances are much smaller (R_{ct} is around 20 times lower and R_{diff} is 50 times up to 2 magnitudes lower than that of the BiF_3 side). Hereby, it is confirmed that the measured kinetics in $BiF_3|BaSnF_4|Sn$ cells predominately reflect the behavior of the BiF_3 cathode.

As can be seen in Fig. 5a and b, across three pressure conditions, the dominant SOC-dependent processes in the BiF_3 cathode composite are charge transfer (resistance referred to as R_{ct}) and ion diffusion processes (R_{diff}). Here, F^- diffusion is considered to be the primary contribution due to the minor fraction of the oxygen impurity and much slower oxygen accumulation (predominantly along solid–solid interfaces).[32] Similarly, it has been reported for oxide electrode materials such as $Li_7Ti_5O_{12}$ (LTO) in LIBs that those two processes are kinetically dominant and are sensitive to the SOC. Thus, we conclude that the charge transfer and diffusion processes exhibit relatively high resistance values at the beginning of discharge, which can be attributed to the activation process, the low concentration of F^- defects in the fully charged BiF_3 lattice and the nucleation of the metallic Bi phase. Reversibly, the increase in R_{diff} and R_{ct} at the end of charging results from the reduced availability of F^- defects and the poor electronic conductivity of BiF_3 [46] and oxidefluorides,[47,48] once present, compared to metallic Bi and CNF. As described in the previous chapter, the formation of oxidefluoride phases (*e.g.*, BiOF and $BiO_{0.1}F_{2.8}$) is generally suppressed under the pressure conditions investigated in this work. Correspondingly, the associated R_{int} remains small during cycling and relatively stable during discharge. However, R_{int} exhibits a pronounced increase during charging, particularly for later SOCs (see the discussion later in this chapter).

With increasing stack pressure, R_{diff}, R_{ct} and R_{int} all decrease significantly from moderate (20 MPa) to high pressure (180 MPa), primarily due to drastically improved solid–solid interparticle contact. However, at the highest pressure investigated (430 MPa), only a minor impact of resistance reduction can be observed, while other effects, such as lattice distortion and pressure-induced phase evolution, become dominant under this condition.

Notably, during the first defluorination, R_{diff} shows a complex behavior with two minima, in agreement with three stages of structural evolution as described in our previous study.[32] With F^- extraction and Bi formation, orthorhombic BiF_3 transitions to cubic BiF_{3-x}, then an orthorhombically distorted phase is formed prior to the formation of Bi metal becoming predominant (referred to as Stage I, II and III marked in Fig. 5a). It can be clearly seen that in Stage I R_{diff} decreases during the transition from o-BiF_3 to c-BiF_3, then increases in stage II with o′-$BiF_{3-\delta}$ increasing its fraction. Finally, in Stage III, R_{diff} decreases when the phase fraction of o′-$BiF_{3-\delta}$ decreases again. Considering that F^- diffusion within the grain of Bi-containing active materials occurs mainly through a vacancy-exchange mechanism, an increase in F^- vacancy concentration would initially enhance the ion mobility. Once the amount of F^- defects reaches a certain threshold, the defects tend to cluster, leading to structural distortion, and this appears to increase the resistance for F^- within the electrode.

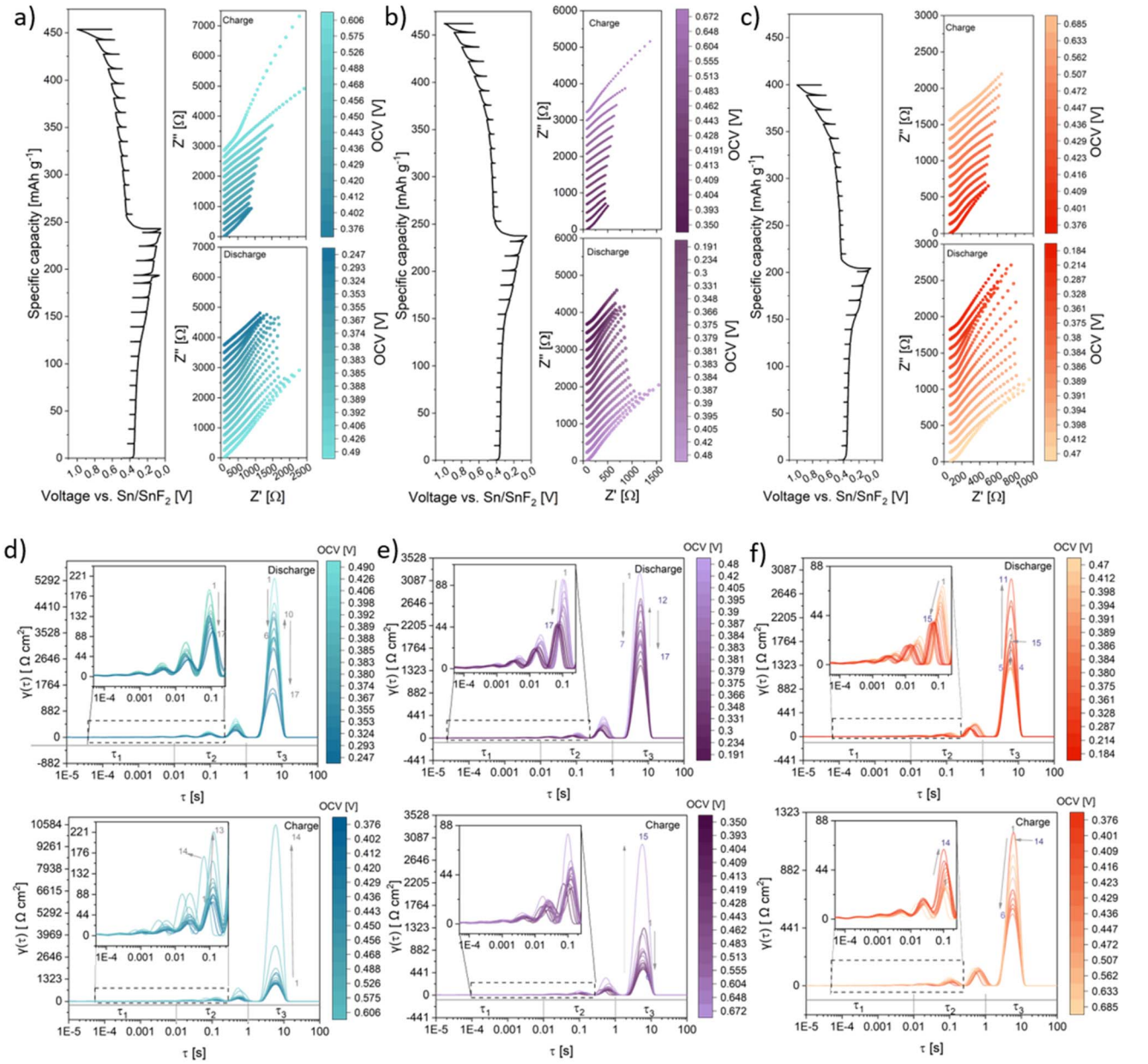

Fig. 4 *In situ* EIS-DRT analysis of the BiF_3|$BaSnF_4$|Sn cells under stack pressures. (a) 22 MPa: (left) voltage profile with selected SOCs and (right) corresponding Nyquist plots during discharge and charge; (b) 180 MPa: (left) Voltage profile with selected SOCs and (right) corresponding Nyquist plots during discharge and charge; (c) 430 MPa: (left) Voltage profile with selected SOCs and (right) corresponding Nyquist plots during discharge and charge; (d–f) corresponding DRT patterns of the cells in (a–c) with specific time constant regimes indicated (SE resistance is determined by the intercept of Nyquist plots at the real impedance axis and is not included in DRT analysis due to the absence of a semicircle).

This change is observed independent of stack pressure, indicating that this partial defluorination mechanism is intrinsic to the BiF_3 cathode. In the subsequent fluorination on charging, R_{diff} only possesses a single minimum observed at OCVs between 0.35 and 0.45 V, coinciding with the formation of o′-$BiF_{3-\delta}$ at the beginning of fluorination. R_{diff} then increases again as fluorination proceeds *via* formation of c-BiF_{3-x} from o′-$BiF_{3-\delta}$, consistent with the reversible phase transformation observed by *operando* and *ex situ* XRD. Noticeably, over Stage II to III of defluorination, R_{diff} increases at 430 MPa and even exceeds the value under 180 MPa, being even 1.5 times higher than that before cycling. Given the defect-richer nature of the intermediate o′-$BiF_{3-\delta}$ phase in this region, it is plausible that this modification exhibits a distinct activation volume, making the F^- mobility more susceptible to the pressure effect than in other modifications. This could be considered the most plausible origin for the capacity degradation described in Fig. 1b. This is also in agreement with the increased R_{diff} under 430 MPa during charging in the OCV range from 0.35 to 0.5 V. Overall, these findings indicate that, despite enhanced interparticle contact at high stack pressures, which should facilitate charge transport, excessive pressure may instead negatively affect the

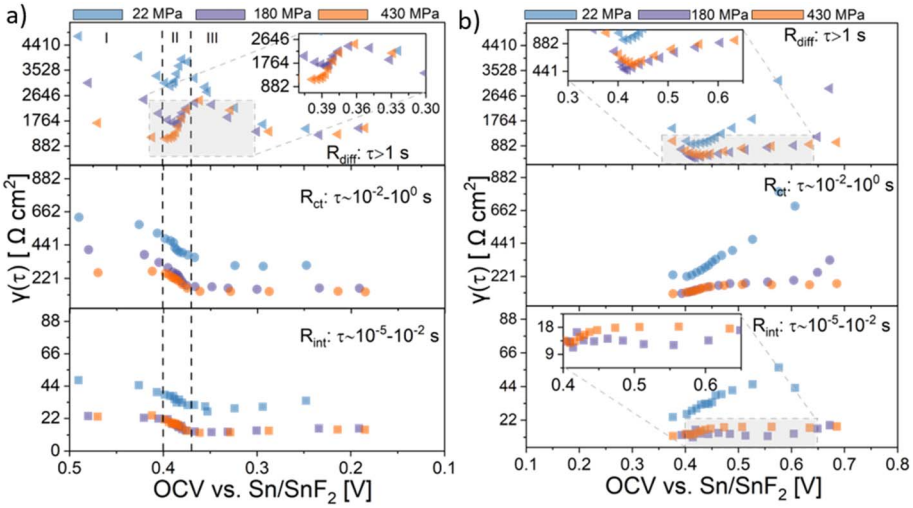

Fig. 5 Fitted resistances of the cells in Fig. 4a–c (interphase, charge transfer and diffusion through Bi-containing electrode active materials (CAMs)) categorized according to their characteristic time constants.

F^- ion mobility within defect-rich phases of the Bi/BiF_3 cathode. We also note that the suppression of F^- mobility aligns well with the increased formation of $BiO_{0.1}F_{2.8}$ under pressure beyond 200 MPa (see Section 3.2), likely arising from the competitive F^- and O^{2-} diffusion kinetics. This also explains the higher R_{int} observed at 430 MPa compared to 180 MPa (Fig. 5b). Overall, the DRT study in combination with diffraction analysis shows that the stack pressure must be carefully optimized to balance between improved interfacial contact and adverse effects on ionic transport and phase stability.

4 Conclusions

In this work, we systematically investigated the effects of stack pressure on the electrochemical performance, phase evolution and kinetic behavior of a BiF_3 cathode in all-solid-state fluoride-ion batteries (ASSFIBs), using $BaSnF_4$ as the solid electrolyte. By integrating galvanostatic cycling, *operando* & *ex situ* XRD, and *in situ* EIS-DRT analysis under varied stack pressures, we revealed a multifaceted pressure-dependent behavior that determines both thermodynamic aspects of phase formation and kinetic processes of ion transport within the cathode composite.

Our results demonstrated that applying high pressures (150–180 MPa) significantly improves cell capacity, coulombic efficiency, and long-term cycling stability. This enhancement is not only attributed to the improved mechanical contact between solid–solid interfaces and the increased ionic conductivity of $BaSnF_4$, which reduces the cell overpotential and collectively preserves electronic and ionic percolation pathways, but also to the suppression of the formation of oxygen-rich BiOF and corresponding interfacial degradation. In contrast, cells under insufficient pressure suffer from interfacial degradation, including delamination and collective oxidefluoride formation (BiOF or $BiO_{0.1}F_{2.8}$), explaining the rapid capacity decay; the XRD result reveals that excessive pressures beyond 200 MPa lead to increased $BiO_{0.1}F_{2.8}$ formation, by suppressing F^- mobility and promoting competitive diffusion with oxygen impurities. While optimized stack pressure hinders oxygen accumulation, the related interfacial degradation due to residual oxygen impurity remains unavoidable during prolonged cycling, emphasizing the critical need for electrolyte purification and interface design.

Through *in situ* EIS-DRT analysis, we identified different kinetic processes and correlated them to the observed phase evolution and capacity decay. It is revealed that charge transfer and ion diffusion within Bi-containing active materials are the dominant SOC-dependent kinetic processes. The resistance contributions R_{diff} and R_{ct} exhibit strong correlation with structural evolution, evidenced by the observed changes of R_{diff} during defluorination and fluorination, respectively, highlighting the intrinsic nature of phase-change-driven F^- mobility in BiF_3. Moreover, excessive stack pressure (430 MPa) was found to suppress F^- mobility, particularly at defect-rich stages.

Overall, our findings demonstrate that the influence of stack pressure on ASSFIBs is non-monotonic and governed by a complex interplay between mechanical contact, competing ion transport and phase evolution. Careful optimization of stack pressure is essential to balance mechanical stability, ionic transport and phase reversibility, and to ensure high-performance fluoride-ion battery systems.

Author contributions

H. C. carried out the synthesis of the precursors and preparation of the electrochemical cells and samples for further characterization measurements such as *operando* and *ex situ* XRD and *in situ* EIS measurements, performed *ex situ* and *operando* XRD measurements and *in situ* EIS measurements, analyzed XRD, EIS(DRT) and GCPL data including plotting of data, and wrote the manuscript. P. B. carried out the synthesis of the precursors and preparation of the electrochemical cells and samples for GCPL measurement under various stack pressures

for 1 cycle, and conducted GCPL measurements for further characterization under the supervision of H. C. O. C. guided and supervised the project, and contributed to writing the manuscript.

Conflicts of interest

There are no conflicts of interest to declare.

Data availability

Crystallographic data for o-BiF_3 *Pnma* has been deposited at the ICSD under 1269 and can be obtained from https://doi.org/10.1002/zaac.19774360112.

Crystallographic data for c-BiF_3 *Fm*-3*m* has been deposited at the ICSD under 24522 and can be obtained from https://icsd.fiz-karlsruhe.de/display/details.xhtml.

Crystallographic data for Bi has been deposited at the ICSD under 64703 and can be obtained from https://doi.org/10.1107/S0365110X62002297.

Crystallographic data for BiOF has been deposited at the ICSD under 24096 and can be obtained from https://icsd.fiz-karlsruhe.de/display/details.xhtml.

Crystallographic data for BiF_3 *P*-3*c* has been deposited at the ICSD under 29325 and can be obtained from https://doi.org/10.1088/1742-6596/871/1/012007.

Crystallographic data for $BiO_{0.1}F_{2.8}$ *P*4/*nmm* has been deposited at the ICSD under 24056 and can be obtained from https://icsd.fiz-karlsruhe.de/display/details.xhtml.

Crystallographic data for $BaSnF_4$ *P*4/*nmm* has been deposited at the ICSD under 166207 and can be obtained from https://doi.org/10.1063/1.3234393.

The data supporting this article have been included as part of the supplementary information (SI). Supplementary information is available. See DOI: https://doi.org/10.1039/d5ta06611e.

References

1 V. K. Davis, C. M. Bates, K. Omichi, B. M. Savoie, N. Momčilović, Q. Xu, W. J. Wolf, M. A. Webb, K. J. Billings, N. H. Chou, S. Alayoglu, R. K. McKenney, I. M. Darolles, N. G. Nair, A. Hightower, D. Rosenberg, M. Ahmed, C. J. Brooks, T. F. Miller, R. H. Grubbs and S. C. Jones, Room-temperature cycling of metal fluoride electrodes: Liquid electrolytes for high-energy fluoride ion cells, *Science*, 2018, **362**(6419), 1144–1148.

2 A. PotaninA. Patent 7722993 B2. 2010.

3 M. A. Nowroozi, S. Ivlev, J. Rohrer and O. Clemens, La_2CoO_4: a new intercalation based cathode material for fluoride ion batteries with improved cycling stability, *J. Mater. Chem. A*, 2018, **6**(11), 4658–4669.

4 M. A. Nowroozi, K. Wissel, M. Donzelli, N. Hosseinpourkahvaz, S. Plana-Ruiz, U. Kolb, R. Schoch, M. Bauer, A. M. Malik, J. Rohrer, S. Ivlev, F. Kraus and O. Clemens, High cycle life all-solid-state fluoride ion battery with La_2NiO_{4+d} high voltage cathode, *Commun. Mater.*, 2020, **1**, 27.

5 V. Vanita, A. I. Waidha, S. Vasala, P. Puphal, R. Schoch, P. Glatzel, M. Bauer and O. Clemens, Insights into the first multi-transition-metal containing Ruddlesden–Popper-type cathode for all-solid-state fluoride ion batteries, *J. Mater. Chem. A*, 2024, **12**(15), 8769–8784.

6 K. Wissel, R. Schoch, T. Vogel, M. Donzelli, G. Matveeva, U. Kolb, M. Bauer, P. R. Slater and O. Clemens, Electrochemical Reduction and Oxidation of Ruddlesden–Popper-Type $La_2NiO_3F_2$ within Fluoride-Ion Batteries, *Chem. Mater.*, 2021, **33**(2), 499–512.

7 V. Vanita, G. Mezzadra, C. Tealdi and O. Clemens, Fluoride Ion Transport and Phase Evolution in the Cathode Material $LaSrMnO_4$ within All-Solid-State Fluoride Ion Batteries, *ACS Appl. Energy Mater.*, 2025, **8**(11), 7562–7574.

8 N. Ohta, K. Takada, I. Sakaguchi, L. Zhang, R. Ma, K. Fukuda, M. Osada and T. Sasaki, $LiNbO_3$-coated $LiCoO_2$ as cathode material for all solid-state lithium secondary batteries, *Electrochem. Commun.*, 2007, **9**(7), 1486–1490.

9 N. Ohta, K. Takada, L. Zhang, R. Ma, M. Osada and T. Sasaki, Enhancement of the High-Rate Capability of Solid-State Lithium Batteries by Nanoscale Interfacial Modification, *Adv. Mater.*, 2006, **18**(17), 2226–2229.

10 W. Zhang, D. Schröder, T. Arlt, I. Manke, R. Koerver, R. Pinedo, D. A. Weber, J. Sann, W. G. Zeier and J. Janek, Electrochemical expansion during cycling: monitoring the pressure changes in operating solid-state lithium batteries, *J. Mater. Chem. A*, 2017, **5**(20), 9929–9936.

11 R. Koerver, I. Aygün, T. Leichtweiß, C. Dietrich, W. Zhang, J. O. Binder, P. Hartmann, W. G. Zeier and J. Janek, Capacity Fade in Solid-State Batteries: Interphase Formation and Chemomechanical Processes in Nickel-Rich Layered Oxide Cathodes and Lithium Thiophosphate Solid Electrolytes, *Chem. Mater.*, 2017, **29**(13), 5574–5582.

12 J. Janek and W. G. Zeier, A solid future for battery development, *Nat. Energy*, 2016, **1**(9), 16141.

13 Y. Kato, S. Hori, T. Saito, K. Suzuki, M. Hirayama, A. Mitsui, M. Yonemura, H. Iba and R. Kanno, High-power all-solid-state batteries using sulfide superionic conductors, *Nat. Energy*, 2016, **1**(4), 16030.

14 W. Zhang, D. A. Weber, H. Weigand, T. Arlt, I. Manke, D. Schröder, R. Koerver, T. Leichtweiss, P. Hartmann, W. G. Zeier and J. Janek, Interfacial Processes and Influence of Composite Cathode Microstructure Controlling the Performance of All-Solid-State Lithium Batteries, *ACS Appl. Mater. Interfaces*, 2017, **9**(21), 17835–17845.

15 A. Sakuda, A. Hayashi and M. Tatsumisago, Interfacial Observation between $LiCoO_2$ Electrode and Li_2S—P_2S_5 Solid Electrolytes of All-Solid-State Lithium Secondary Batteries Using Transmission Electron Microscopy, *Chem. Mater.*, 2010, **22**(3), 949–956.

16 K. H. Park, D. Y. Oh, Y. E. Choi, Y. J. Nam, L. Han, J.-Y. Kim, H. Xin, F. Lin, S. M. Oh and Y. S. Jung, Solution-Processable Glass LiI-Li_4SnS_4 Superionic Conductors for All-Solid-State Li-Ion Batteries, *Adv. Mater.*, 2016, **28**(9), 1874–1883.

17 M. Nagao, A. Hayashi and M. Tatsumisago, High-capacity Li_2S–nanocarbon composite electrode for all-solid-state rechargeable lithium batteries, *J. Mater. Chem.*, 2012, **22**(19), 10015–10020.
18 H. Chen, T. Aalto, V. Vanita and O. Clemens, Effect of Uniaxial Stack Pressure on the Performance of Nanocrystalline Electrolytes and Electrode Composites for All-Solid-State Fluoride-Ion Batteries, *Small Struct.*, 2024, **5**(7), 2300570.
19 W. Liu, Y. Luo, Y. Hu, Z. Chen, Q. Wang, Y. Chen, N. Iqbal and D. Mitlin, Interrelation Between External Pressure, SEI Structure, and Electrodeposit Morphology in an Anode-Free Lithium Metal Battery, *Adv. Energy Mater.*, 2024, **14**(5), 2302261.
20 C. Wei, C. Liu, Y. Xiao, Y. Li, Z. Jiang, X. Liang, K. Cao, S. Cheng, Y. Huang and C. Yu, Pressure Tuning and Sn Particle Size Optimization for Enhanced Performance in $PbSnF_4$-Based All-Solid-State Fluoride Ion Batteries, *Small*, 2024, **20**, 2401502.
21 X. Gao, B. Liu, B. Hu, Z. Ning, D. S. Jolly, S. Zhang, J. Perera, J. Bu, J. Liu, C. Doerrer, E. Darnbrough, D. Armstrong, P. S. Grant and P. G. Bruce, Solid-state lithium battery cathodes operating at low pressures, *Joule*, 2022, **6**(3), 636–646.
22 B. Liu, S. D. Pu, C. Doerrer, D. Spencer Jolly, R. A. House, D. L. R. Melvin, P. Adamson, P. S. Grant, X. Gao and P. G. Bruce, The effect of volume change and stack pressure on solid-state battery cathodes, *SusMat*, 2023, **3**(5), 721–728.
23 C. Lee, J. Y. Kim, K. Y. Bae, T. Kim, S.-J. Jung, S. Son and H.-W. Lee, Enhancing electrochemomechanics: How stack pressure regulation affects all-solid-state batteries, *Energy Storage Mater.*, 2024, **66**, 103196.
24 J. Sakabe, N. Ohta, T. Ohnishi, K. Mitsuishi and K. Takada, Porous amorphous silicon film anodes for high-capacity and stable all-solid-state lithium batteries, *Commun. Chem.*, 2018, **1**(1), 24.
25 D. H. S. Tan, Y.-T. Chen, H. Yang, W. Bao, B. Sreenarayanan, J.-M. Doux, W. Li, B. Lu, S.-Y. Ham, B. Sayahpour, J. Scharf, E. A. Wu, G. Deysher, H. E. Han, H. J. Hah, H. Jeong, J. B. Lee, Z. Chen and Y. S. Meng, Carbon-free high-loading silicon anodes enabled by sulfide solid electrolytes, *Science*, 2021, **373**(6562), 1494–1499.
26 P. Lu, Y. Wu, D. Wu, F. Song, T. Ma, W. Yan, X. Zhu, F. Guo, J. Lu, J. Peng, L. Chen, H. Li and F. Wu, Rate-limiting mechanism of all-solid-state battery unravelled by low-temperature test-analysis flow, *Energy Storage Mater.*, 2024, **67**, 103316.
27 Y. Lu, C.-Z. Zhao, J.-Q. Huang and Q. Zhang, The timescale identification decoupling complicated kinetic processes in lithium batteries, *Joule*, 2022, **6**(6), 1172–1198.
28 R. Zhang, A. Kondrakov, J. Janek and T. Brezesinski, Timescale Identification of Electrochemical Processes in All-Solid-State Batteries Using an Advanced Three-Electrode Cell Setup, *Energy Storage Mater.*, 2025, 104000.
29 L. Li, C. Fang, W. Wei, L. Zhang, Z. Ye, G. He and Y. Huang, Nano-ordered structure regulation in delithiated Si anode triggered by homogeneous and stable Li-ion diffusion at the interface, *Nano Energy*, 2020, **72**, 104651.
30 R. Soni, J. B. Robinson, P. R. Shearing, D. J. L. Brett, A. J. E. Rettie and T. S. Miller, Lithium-sulfur battery diagnostics through distribution of relaxation times analysis, *Energy Storage Mater.*, 2022, **51**, 97–107.
31 I. Mohammad, R. Witter, M. Fichtner and M. Anji Reddy, Room-temperature, rechargeable solid-state fluoride-ion batteries, *ACS Appl. Energy Mater.*, 2018, **1**(9), 4766–4775.
32 H. Chen, R. Schoch, J.-N. Chotard, Y. M. Thiebes, K. Wissel, R. Niewa, M. Bauer and O. Clemens, Revealing an Intercalation Nature of High-Capacity Conversion Cathode Materials for Fluoride-Ion Batteries by Operando Studies, *Small Methods*, 2025, **9**(8), 2500374.
33 J. Perl, J. Shin, J. Schumann, B. Faddegon and H. Paganetti, TOPAS: an innovative proton Monte Carlo platform for research and clinical applications, *Med. Phys.*, 2012, **39**(11), 6818–6837.
34 U. Croatto, Edifici cristallini con disordine reticolare. Fluoruro di piombo e bismuto, *Gazz. Chim. Ital.*, 1944, **74**, 20.
35 B. Aurivillius, C. Brosset, T. Ledaal and H. Seip, The Crystal Structure of Bismuth Oxide Fluoride, *Acta Chem. Scand.*, 1964, **18**(8), 1823–1830.
36 P. Cucka and C. S. Barrett, The crystal structure of Bi and of solid solutions of Pb, Sn, Sb and Te in Bi, *Acta Crystallogr.*, 1962, **15**(9), 865–872.
37 O. M.-R. Greis and M. Darstellung, Temperaturverhalten und Kristallstruktur von BiF_3, *Z. Anorg. Chem.*, 1977, **436**, 105–112.
38 C. Schneider, C. P. Schmidt, A. Neumann, M. Clausnitzer, M. Sadowski, S. Harm, C. Meier, T. Danner, K. Albe, A. Latz, W. A. Wall and B. V. Lotsch, Effect of Particle Size and Pressure on the Transport Properties of the Fast Ion Conductor t-Li7SiPS8, *Adv. Energy Mater.*, 2023, **13**(15), 2203873.
39 Y. Lu, X. Huang, Y. Ruan, Q. Wang, R. Kun, J. Yang and Z. Wen, An *in situ* element permeation constructed high endurance Li–LLZO interface at high current densities, *J. Mater. Chem. A*, 2018, **6**(39), 18853–18858.
40 O. Hassel and S. Nilssen, Der Kristallbau des BiF_3, *Z. Anorg. Allg. Chem.*, 1929, **181**(1), 172–176.
41 F. Hund and R. Fricke, Der Kristallbau von α-BiF_3, *Z. Anorg. Chem.*, 1949, **258**(3–5), 198–204.
42 N. I. Sorokin and D. N. Karimov, Ionic Conductivity and Thermal Stability of BiF_3 Crystals, *KG*, 2023, **68**(2), 285–289.
43 K. Nagasaka, G. Jinno, O. Miura, A. Miura, C. Moriyoshi, Y. Kuroiwa and Y. Mizuguchi, Synchrotron powder X-ray diffraction and structural analysis of $Eu_{0.5}La_{0.5}FBiS_{2-x}Se_x$, *J. Phys.: Conf. Ser.*, 2017, **871**(1), 012007.
44 S. R. G. Christopoulos, A. Kordatos, M. W. D. Cooper, M. E. Fitzpatrick and A. Chroneos, Activation volumes of oxygen self-diffusion in fluorite structured oxides, *Mater. Res. Express*, 2016, **3**(10), 105504.
45 E. T. Park, . J.-H. Park In *Pressure Effecton Ionic Condaty in Yttrium-Oxide-Doped Single-Crystal Zirconium Oxide*, 3rd

International Meeting of Pacific Rim Ceramic Societies, 1998.
46 J. Liu, Z. Zang, L. Yi, P. Zeng, C. Zou, X. Chen, X. Tao, L. Yang, B. Chang, Y. Shen and X. Wang, Constructing a BiF3/Bi7F11O5 multiple-phase composite as advanced cathode for room-temperature all-solid-state fluoride-ion batteries, *J. Electroanal. Chem.*, 2023, **928**, 117073.
47 J. Ning, W. Meng, C. Wang, H. Wang, C. Wu, L. You, X. Wang, Y. Pei, H. Wang and Z. Yang, Structure design of a BiOF solid electrolyte with remarkably outstanding fluoride ion diffusion performance induced by Ga doping, *J. Mater. Chem. A*, 2024, **12**(26), 15592–15600.
48 N. I. Sorokin and B. P. Sobolev, Ionic conductivity of bismuth oxofluoride $BiO_{0.1}F_{2.8}$ with tysonite-type structure (LaF_3), *Russ. J. Electrochem.*, 2011, **47**(1), 111–113.